Novel incident angle modifier model for quasi-dynamic testing of flat plate solar thermal collectors

J. M. Rodríguez-Muñoz[a,*], I. Bove[b], R. Alonso-Suárez[b]

[a] *Laboratorio de Energía Solar, Centro Universitario Regional Litoral Norte, Av. L. Batlle Berres km 508, Salto, Uruguay*
[b] *Laboratorio de Energía Solar, Instituto de Física, Facultad de Ingeniería, J. H. y Reissig 565, Montevideo, Uruguay*

Abstract

There are two accepted standard methodologies to characterize the performance of solar thermal collectors: Steady-State Testing (SST) and Quasi-Dynamic Testing (QDT). This last methodology requires a model for the Incident Angle Modifier (IAM). In this article a new model for the IAM is presented to be used in the quasi-dynamic testing of Flat Plate Collectors (FPC), inspired in the interpolation procedure indicated by the ISO-9806 (2017) standard for SST. The model considers the IAM as a continuous and piecewise linear function and uses its nodes values at each 10° as adjustable parameters. The model's performance is compared against four other widely-used pre-existing models, being more precise and showing a better overall agreement in the whole incident angle's range. It is observed that the proposal is also more reliable, as it has a lower sensitivity to experimental data variability. This second characteristic allows to reduce test's duration because it eliminates the ISO-9806 (2017) requirement of testing the collector in the morning and afternoon, in a balanced manner. Although the specific implementation of this work is for FPC, the model can be extended to other solar collector technologies as it has the ability to represent the IAM variability for all incident angles.

Keywords: Flat plate collectors, incident angle modifier, quasi-dynamic testing, ISO 9806 standard.

---

1. Introduction

The energy efficiency test of solar thermal collectors allows to determine the main parameters of their thermodynamic behavior. The models resulting from this characterization can be used to estimate the useful energy that the equipment will produce in annual or monthly terms, typically, from simulations of higher temporal resolution (hourly or 10-minute) that take meteorological and utilization data as input for the location and specific application. The ISO-9806 (2017) standard is one of the most used to characterize the thermal performance of solar collectors since it covers a wide variety of technologies: uncovered collectors, flat plate, vacuum tubes, concentrating collectors, etc. This standard admits two test methodologies: one in

[*] Corresp. author: J. M. Rodríguez-Muñoz, jrodrigue@fing.edu.uy

Steady State Testing (SST), where a high stability of the system forces is required (flow rate and temperature at the inlet, solar irradiance, wind speed, etc.), and the other in Quasi-Dynamic Testing (QDT), in which the stability conditions are more flexible. In various publications the equivalence between both methodologies has been shown, to cite a few: Fischer et al. (2004), Kratzenberg et al. (2006), Rojas et al. (2008), García de Jalón et al. (2011), Osório & Carvalho (2014), Rodríguez-Muñoz et al. (2020).

This work focuses on the modeling of the Incident Angle Modifier (IAM, see its definition in Section 2) for the QDT methodology. This methodology requires the collector to experience various operating conditions during the test time. This variability in operating conditions is achieved by varying the inlet flow temperature and exposing the collector to operate under different sky conditions (clear sky, partially cloudy sky, and completely overcast sky). The determination of all characteristic parameters of the collector is done simultaneously by using Multi-Linear Regression (MLR). There are previous works in which non-linear regression techniques and dynamic simulations have been used together to determine these parameters (Muschaweck & Spirkl, 1993), although their use is not widespread. In either case, whether linear or nonlinear regression is used, a model must be chosen for the IAM. This quantity is usually modeled as an empirical function of the incident angle, θ, and the expression takes the form of an adjustable parameterization. If the adjustment of the parameters is done through multi-linear regression, then the IAM model used must be linear with respect to the parameters.

Several empirical models have been proposed for the IAM. The ISO-9806 (2017) standard suggest one method in particular, known as Ambrosetti function. Its utilization for an standard QDT requires a non linear regression algorithm and has not been reported yet, aside the work of Muschaweck & Spirkl (1993) in which a dynamic in-situ testing is used. Another model, widely-used for Flat Plate Collectors (FPC) with one cover, is that of Souka & Safwat (1966), which has a single adjustable parameter through linear regression. Two improved variations of this model were proposed by incorporating a second adjustable parameter, a linear model (Kalogirou, 2004) and a non-linear model (Tesfamichael & Wäckelgård, 2000), whose use extends to FPC with two covers. Perers (1997) proposed a piecewise model that assumes a constant IAM value for each incident angle interval, and thus, there is an adjustable parameter for each defined interval. This model was initially tested for FPC and has the disadvantage that if there are large IAM variations within a certain interval, then the error of the model in that interval will also be large. This model has also been successfully used in flat collectors with CPC reflectors (Rönnelid et al., 1997). For vacuum tube collectors the problem is more complex as the IAM is a function of two incident angles: θ_L and θ_T. An important simplification to this problem was introduced by McIntire (1982), which consists in factoring the IAM, that is, writing it as the product of two functions, one dependent on θ_L and the other on θ_T. Osório & Carvalho (2014) uses this simplification to test vacuum tube collectors with the QDT method, using the Souka & Safwat model for the θ_L dependent function and the Perers model for the θ_T dependent function. Zambolin & Del Col (2012), considering the large variation of the θ_T dependent function and that the Perers model does not fit quite well, proposed a generalization of the Souka & Safwat model for this component by adding 3 adjustable coefficients (4 in total). For concentrating collectors, some specific IAM empirical models were developed (Kalogirou, 2004; Eck et al., 2014), which can be used for linear QDT as they are linear with respect to their parameters. In the SST it is valid to determine the IAM for certain incident angles (which we shall call nodes), and then linearly interpolate between them. In this sense, the ISO-9806 (2017) standard proposes an equation to perform this interpolation.

This article presents a new model for the IAM to be used in the QDT of FPC using multi-linear regression. The model consists in building the IAM up by a continuous and piecewise linear function. For this, the interpolation equation provided by the ISO-9806 (2017) standard for SST is generalized as a model (parametrization) for the QDT case, using the eight inner node values as adjustable parameters. This changes fundamentally the way this equation is used, as for the SST case it is just a way to linearly interpolate between directly measured IAM data at given incident angles, and for this proposal it is used as IAM model whose parameters are determined by linear regression at the same time with the other collector's parameters. This model can be seen as an improvement of the Perers model, given that both models have some similarities, such as, for example, that the range of incident angles must be partitioned and that dummy functions must be used to adjust the parameters to the experimental data. These dummy functions are such that they take the value of 1 if a certain variable belongs to a category and 0 if not. The main advantage of the proposed model compared to the previous ones is that it is more precise, in particular, in the intervals of incident angles where the IAM presents large variations. This property makes the model an attractive choice to be used in the testing of vacuum tube solar collectors, which have a more complex IAM. Another advantage of the novel model is that it is more reliable against experimental uncertainty, since its parameters are not very sensitive to variations in the measurements. Furthermore, we think that the proposed model can eliminate the requirement of the ISO-9806 (2017) standard to have measurements before and after solar noon, which increases the duration of the tests. This article shows the implementation of this new model and validates it for a reference FPC. Using a set of independent data, its performance is evaluated, and the sensitivity of the characteristic parameters against the variation of the experimental data is analyzed. The performance of this model is compared with that of the ISO-9806 (2017); Souka & Safwat (1966); Kalogirou (2004); Perers (1997) models. The use of the Kalogirou model for the QDT methodology has not yet been analyzed in the literature, which is another contribution of this work.

This article is organized as follows. Section 2 describes the thermal model presented in the ISO-9806 (2017) standard for quasi-dynamic testing of low temperature solar collectors with cover (flat plate collectors are included in this category) and shows the implementation of the different IAM models (parameter identification procedure). Section 3 describes the test facility, the measurements taken, and the adjustment and evaluation methodology of the different models. Section 4 presents and discusses the results. Finally, Section 5 summarizes the main conclusions of this work.

2. Collector model and parameter identification procedure

This section describes the thermal model used in the quasi-dynamic testing of FPC, the different incidence angle modifier models and the parameter identification procedure.

2.1. Model for quasi-dynamic testing

The thermal model considered by the quasi-dynamic method of the ISO-9806 (2017) standard is quite general and can be applied to different technologies of thermal solar collectors. The standard provides criteria on how to use the model in each case, that is, which terms can be omitted in the general equation depending on the solar collector technology. Eq. (1) shows the suggested model for low temperature collectors with cover,

$$\frac{\dot{Q}_u}{A_G} = \eta_{0,b}\left[K_b\left(\theta\right)\ G_{bt} + K_d\ G_{dt}\right] - a_1\left(\vartheta_m - \vartheta_a\right) - a_2\left(\vartheta_m - \vartheta_a\right)^2 - \frac{C}{A_G}\frac{d\vartheta_m}{dt}, \tag{1}$$

where G_{bt} and G_{dt} are the direct and diffuse solar irradiance on the collector plane, respectively, and the parameters that characterize the thermal behavior of the collector are: $\eta_{0,b}$, K_b, K_d, a_1, a_2 and C. The meaning and unit of each parameter, including A_G, are indicated in nomenclature list.

The $\eta_{0,b}$ peak efficiency corresponds to the product of the efficiency factor and the optical efficiency of the collector at normal incidence, that is, $\eta_{0,b} = F'\left(\tau\alpha\right)_n$. It should be noted that, for uniformity with other articles and textbooks, the nomenclature used in this work is not exactly the one used by ISO-9806 (2017) standard for the QDT, however, the parameters have the same meaning. All the characteristic parameters of the collector are assumed to be constant except for the incident angle modifier for direct solar irradiance (K_b), which is modeled as a function of the incident angle.

2.2. Incident angle modifier (IAM)

The incident angle modifier for direct solar irradiance is defined as the ratio between the peak efficiency at a given incident angle, $\eta_b(\theta)$, and the peak efficiency at normal incidence to the collector plane ($\theta = 0°$), $\eta_{0,b}$:

$$K_b\left(\theta\right) = \frac{\eta_b(\theta)}{\eta_{0,b}}. \tag{2}$$

In the case of FPC, K_b is a function dependent only on the incident angle θ (univariate function). In this article, five models for this function are considered.

The first model is given in Eq. (3) and corresponds to the one suggested by the standard ISO-9806 (2017). This model has a single adjustable parameter, n, which has a non linear dependency with the IAM, and so, must be determined by non linear regression for QDT. The rest of the models considered in this work are linear with respect to their parameters, which can be determined by a simple linear regression.

$$K_b(\theta) = 1 - \tan^n(\theta/2). \tag{3}$$

The second model is given in Eq. (4) and corresponds to the Souka & Safwat (1966) model. This model has a single adjustable parameter, b_0, and has been widely-used in the quasi-dynamic testing of FPC (Fischer et al., 2004; Kratzenberg et al., 2006; Rojas et al., 2008; Kong et al., 2012; Osório & Carvalho, 2014; Rodríguez-Muñoz et al., 2020).

$$K_b(\theta) = 1 - b_0\left(\frac{1}{\cos\theta} - 1\right). \tag{4}$$

The third model is that of Kalogirou (2004), represented by Eq. (5). This model incorporates an additional quadratic term in the variable $(1/\cos\theta - 1)$ and the adjustable parameters are b_1 and b_2.

$$K_b(\theta) = 1 - b_1\left(\frac{1}{\cos\theta} - 1\right) - b_2\left(\frac{1}{\cos\theta} - 1\right)^2. \tag{5}$$

These three models (ISO-9806, Souka & Safwat and Kalogirou) require that the experimental data (samples) are obtained in a distributed manner throughout the range of variation of the incident angle, ideally, in a uniform manner. Otherwise, the adjustment of the parameters may be biased for one angle range or another, affecting the representativeness of the model throughout the IAM range.

The fourth considered model corresponds to that of Perers (1997), also known as the extended MLR or angle-by-angle method. Like the second model, the model of Perers is widely-used (Rönnelid et al., 1997; Kong et al., 2012; Zambolin & Del Col, 2012; Osório & Carvalho, 2014). As previously mentioned in the introduction, this model consists of a piecewise constant function for incident angle intervals. For example, if a 10° step is used, the adjustable parameters will be $K_b(0^\circ \to 10^\circ), K_b(20^\circ \to 30^\circ), \ldots, K_b(80^\circ \to 90^\circ)$, where $K_b(\theta_i \to \theta_{i+1})$ is the value of K_b (constant) in the interval from θ_i to θ_{i+1}. When there are large variations in K_b, small intervals should be defined to reduce the error of the method. This may result in a large set of experimental data being required, since sufficient data must be available in each of the defined intervals. It should be noted that for the $K_b(\theta_i \to \theta_{i+1})$ value to be similar to the real K_b value at the midpoint of each interval, one must have an approximately uniform distribution of experimental data in each one, and the intervals length must be taken as small enough that a linear behavior can be assumed within them. If within an interval, K_b does not behave in a linear way or the distribution of the samples is not uniform, then this desirable property will not be obtained.

The models described above were selected by their relevance and are used here as reference level to compare the performance of the proposed model. Model 1 is non linear, so it implies a more complex computational implementation than the others, but it is suggested as a reference by the ISO-9806 (2017) for

SST, so it is considered in the comparison although its utilization has not been reported for the standard QDT. Model 2 and 4 are linear, hence simpler to implement, and are widely-used for QDT. Model 3 is an improvement of Model 2 that adds a linear second order term, and its implementation does not represent an extra complexity. This model has also not been tested yet for QDT.

The last model is the one proposed in this work. This model consists in dividing the incident angle range into sub-intervals and assume a piecewise linear function into them. For example, if a 10° step is used, the adjustable parameters will be $K_b(10°), K_b(20°), \ldots, K_b(80°)$, where $K_b(\theta_i)$ corresponds to the K_b value in the θ_i angle (or node). It is imposed for the first and last parameter, respectively, that $K_b(0°) = 1$ and $K_b(90°) = 0$. In the same way as the Perers model, the smaller the angular step, the smaller the model error and the greater the experimental data requirement. The main advantage of this method compared to the previous one is that for the same angular step, a better fit is obtained in the intervals where there are large K_b variations. Another advantage is that, although it is recommended, it is not strictly necessary that the distribution of experimental data in each defined interval to be uniform. The implementation of this proposal requires a little more elaboration than that of the previous linear models, and is described in the next subsection along with the rest of the models.

2.3. Parameter identification procedure

The IAM models described in the previous section can be classified into two groups: (i) linear models and (ii) non linear models. Models from 2 to 5 (Souka & Safwat, Kalogirou, Perers and the novel model) belong to the first group and model 1 (ISO-9806, 2017) to the second. This section describes the parameter identification procedure used for each model, according to their classification. In both cases the measured variables correspond to 5-minutes temporal averages of 10 seconds samples.

2.3.1. Linear IAM models

The parameter identification of Eq. (1) for the linear IAM models is performed by multi-linear regression (MLR). This is done by implementing for each model the standard linear least mean square algorithm with multiple variables. The implementation of the Souka & Safwat model is described in detail in Kratzenberg et al. (2006). Since K_b depends linearly on its only parameter (b_0), the adjustment can be made linearly in terms of the variable $(1/\cos\theta - 1)$. The implementation of the second model is an extension of the first one, adding the independent variable $(1/\cos\theta - 1)^2$ to the linear regression model, so its implementation does not vary significantly. The implementation of the third model is explained in Perers (1997). The adjustment of the Perers model is done through the use of dummy functions. Specifically, a dummy function is applied for each incident angle interval, defined usually by a 10° spacing, and each of these variables will adopt the value of 1 if the incident angle is included in it and 0 if not. Then the parameter adjustment problem can be written as a multi-linear regression, using these functions as variables associated with each adjustable parameter.

The implementation of the proposed model is as follow. If an angular step of 10° is chosen and the K_b values at the nodes are known, 0°, 10°, 20°,. . ., 90°, then the K_b value for any θ angle can be expressed as:

$$K_b(\theta) = \left[K_b\left(\left\lfloor\frac{\theta}{10}\right\rfloor 10\right)\left(\left\lfloor\frac{\theta+10}{10}\right\rfloor - \frac{\theta}{10}\right) + K_b\left(\left\lfloor\frac{\theta}{10}\right\rfloor 10 + 10\right)\left(\frac{\theta}{10} - \left\lfloor\frac{\theta}{10}\right\rfloor\right)\right], \tag{6}$$

where the open square brackets indicate to round up to the previous lower natural number. An advantage of this formulation is that it allows to set the ends of the IAM at physically appropriate values, if $K_b(0^\circ) = 1$ and $K_b(90^\circ) = 0$ are set. This equation corresponds to equation 27 of the ISO-9806 (2017) standard, and is given there for SST as a way to interpolate the IAM data, measured at given incident angles. Therefore, as given by the standard, this simple two-points line determination is not a model itself. Here, in the following paragraphs, it is shown how to include this expression into Eq. (1) to create an IAM model with the nodes $K_b(10^\circ), \ldots, K_b(80^\circ)$ as adjustable parameters. In this way, these parameters are adjusted by linear regression jointly with the other collector's parameters, identically to the other models' formulations.

Applying Eq. (6) to each of the intervals (0°→10°, 10°→20°,. . ., 80°→90°), the term $K_b\ G_{bt}$ of Eq. (1) can be easily written as follows:

$$\begin{aligned} K_b\ G_{bt} =& K_b(0^\circ)\ G_{bt}(0^\circ, 10^\circ)\left(\frac{10-\theta}{10}\right) \\ &+ \sum_{\substack{\phi=10^\circ \\ \text{steps}=10^\circ}}^{80^\circ} K_b(\phi)\left[G_{bt}(\phi-10^\circ, \phi)\left(\frac{\theta-(\phi-10^\circ)}{10}\right) + G_{bt}(\phi, \phi+10^\circ)\left(\frac{(\phi+10^\circ)-\theta}{10}\right)\right] \\ &+ K_b(90^\circ)\ G_{bt}(80^\circ, 90^\circ)\left(\frac{\theta-80}{10}\right), \end{aligned} \tag{7}$$

where the notation $G_{bt}(\phi_1, \phi_2)$, with ϕ_1 and ϕ_2 as two generic angles that satisfy $\phi_2 > \phi_1$, means that $G_{bt} = G_{bt}(\theta)$ if θ belongs to the interval (ϕ_1, ϕ_2), and that $G_{bt} = 0$ otherwise. This function, $G_{bt}(\phi_1, \phi_2)$, can also be seen as a term-by-term product between the vector of measurements G_{bt} and a dummy function that is 1 if θ belongs to the interval (ϕ_1, ϕ_2) or 0 if otherwise. Then, substituting Eq. (7) in Eq. (1), the useful power produced by the collector can be expressed as follows:

$$\begin{aligned} \frac{\dot{Q}_u}{A_G} = \eta_{0,b}\Bigg\{& K_b(0^\circ)\ G_{bt}(0^\circ, 10^\circ)\left(\frac{10-\theta}{10}\right) \\ &+ \sum_{\substack{\phi=10^\circ \\ \text{steps}=10^\circ}}^{80^\circ} K_b(\phi)\left[G_{bt}(\phi-10^\circ, \phi)\left(\frac{\theta-(\phi-10^\circ)}{10}\right) + G_{bt}(\phi, \phi+10^\circ)\left(\frac{(\phi+10^\circ)-\theta}{10}\right)\right] \\ &+ K_b(90^\circ)\ G_{bt}(80^\circ, 90^\circ)\left(\frac{\theta-80}{10}\right)\Bigg\} + \eta_{0,b}K_d\ G_{dt} - a_1\left(\vartheta_m - \vartheta_a\right) - a_2\left(\vartheta_m - \vartheta_a\right)^2 - \frac{C}{A_G}\frac{d\vartheta_m}{dt}. \end{aligned} \tag{8}$$

For the application of the multi-linear regression algorithm, Eq. (8) must be written linearly in terms of its parameters, that is, in the form of $y = \sum_{i=1}^{n} p_i x_i$, where y is the dependent variable, x_i are the independent variables (n in total) and p_i are the parameters to be determined. Thus, the useful power produced by the collector per unit area is defined as the dependent variable ($y = \dot{Q}_u/A_G$) and the independent variables and the coefficients to be determined are listed below:

- $x_1 = G_{bt}(0°, 10°)\left(\frac{10-\theta}{10}\right)$, $p_1 = \eta_{0,b}$,
- $x_2 = \left[G_{bt}(0°, 10°)\left(\frac{\theta}{10}\right) + G_{bt}(10°, 20°)\left(\frac{20-\theta}{10}\right)\right]$, $p_2 = \eta_{0,b}\ K_b(10°)$,
- $x_3 = \left[G_{bt}(10°, 20°)\left(\frac{\theta-10}{10}\right) + G_{bt}(20°, 30°)\left(\frac{30-\theta}{10}\right)\right]$, $p_3 = \eta_{0,b}\ K_b(20°)$,
- $x_4 = \left[G_{bt}(20°, 30°)\left(\frac{\theta-20}{10}\right) + G_{bt}(30°, 40°)\left(\frac{40-\theta}{10}\right)\right]$, $p_4 = \eta_{0,b}\ K_b(30°)$,
- $x_5 = \left[G_{bt}(30°, 40°)\left(\frac{\theta-30}{10}\right) + G_{bt}(40°, 50°)\left(\frac{50-\theta}{10}\right)\right]$, $p_5 = \eta_{0,b}\ K_b(40°)$,
- $x_6 = \left[G_{bt}(40°, 50°)\left(\frac{\theta-40}{10}\right) + G_{bt}(50°, 60°)\left(\frac{60-\theta}{10}\right)\right]$, $p_6 = \eta_{0,b}\ K_b(50°)$,
- $x_7 = \left[G_{bt}(50°, 60°)\left(\frac{\theta-50}{10}\right) + G_{bt}(60°, 70°)\left(\frac{70-\theta}{10}\right)\right]$, $p_7 = \eta_{0,b}\ K_b(60°)$,
- $x_8 = \left[G_{bt}(60°, 70°)\left(\frac{\theta-60}{10}\right) + G_{bt}(70°, 80°)\left(\frac{80-\theta}{10}\right)\right]$, $p_8 = \eta_{0,b}\ K_b(70°)$,
- $x_9 = \left[G_{bt}(70°, 80°)\left(\frac{\theta-70}{10}\right) + G_{bt}(80°, 90°)\left(\frac{90-\theta}{10}\right)\right]$, $p_9 = \eta_{0,b}\ K_b(80°)$,
- $x_{10} = G_{dt}$, $p_{10} = \eta_{0,b}\ K_d$,
- $x_{11} = -(\vartheta_m - \vartheta_a)$, $p_{11} = a_1$,
- $x_{12} = -(\vartheta_m - \vartheta_a)^2$, $p_{12} = a_2$,
- $x_{13} = -\frac{d\vartheta_m}{dt}$, $p_{13} = C/A_G$.

It shall be noted that the values of $K_b(0°)$ and $K_b(90°)$ are not included in the regression problem, since they are imposed at $K_b(0°) = 1$ and $K_b(90°) = 0$. From this point onwards, the problem is solved like any other multiple linear regression problem. The determination of the parameters $p_1, p_2, \ldots, p_{13}$ and the calculation of their respective uncertainties can be consulted in textbooks, for example Quarteroni et al. (2000). The solution of the least mean square algorithm for multiple variables is:

$$p = (X^T X)^{-1} X^T y, \tag{9}$$

where p is a vector containing the parameters' values and X is a matrix with the x_i variables as columns. The uncertainty for each parameter is derived from the covariance matrix, whose detailed calculation can be consulted in Kratzenberg et al. (2006). This is the same procedure that is applied for the parameters' determination in the other linear models. An script (for matlab) that allows to calculate the model's parameters and uncertainty is provided in http://les.edu.uy/RDpub/RBA_model_training.zip.

2.3.2. Non linear IAM model

The parameters identification for model 1 is performed by a non linear least mean square algorithm with multiple variables. There are several ways to address the problem. The procedure used in this work is to linearize the function y^* (estimation of the y variable) around an operating point p_0 as follows:

$$y^*(p) \approx y^*(p_0) + J(p_0)\,(p - p_0)\,, \tag{10}$$

where $J(p_0)$ is the Jacobian matrix of the function $y^*(p)$ evaluated at p_0. The elements of this matrix can be estimated numerically using centered finite differences. Then the problem can be solved iteratively using Eq. (9), substituting the matrix X with $J(p_0)$ and the vector y with $y^*(p_0) - y$. This algorithm is known as Newton's iterative method (Quarteroni et al., 2000). The uncertainty of the parameters can be estimated analogously to the linear case. It is recalled that, as in the previous section (linear models), the temporal derivative of the mean temperature of the fluid ($d\vartheta_m/dt$) is estimated by finite differences using the experimental data and is treated as an independent variable in the regression algorithm.

3. Experimental data and methodology

This section describes the test facility, the measurements performed and the methodology for evaluating the models.

3.1. Test facility

The measurements were taken at the Solar Heaters Test Platform (BECS) of the Solar Energy Laboratory (LES, http://les.edu.uy/) of the Universidad de la República (UdelaR) located near the city of Salto (Latitude=31.28° S, Longitude=57.92° W), Uruguay. This test facility was designed by researchers from this laboratory based on the pre-existing platform of the National Renewable Energy Center (CENER) in Spain. Recently, the BECS participated in a Latin American inter-comparison of test laboratories organized by the PTB (Physikalisch-Technische Bundesanstalt), the German Metrological Institute, an activity in which the platform obtained the best qualification for almost all tests and just one minor observation in the determination of a secondary variable (Fischer, 2020).

A flat plate solar thermal collector with a gross area of $2.02\,\mathrm{m}^2$ was used for this work, which was the reference collector also used in the aforementioned inter-comparison of test laboratories. The measurements were made between November 17th and December 18th, 2019. Some of these measurements were also used for the inter-comparison. The collector was mounted on a mobile tracker as shown in Figure 1. The horizontal tilt of this tracker can be manually adjusted between 5° and 85°, and the azimuth can be adjusted manually or automatically with a 2-minute time step between −90° and 90°.

Figure 1: Assembly of the collector on the solar tracker of the test bank.

Figure 2 shows a simplified diagram of the thermo-hydraulic installation of the BECS. It has three independent circuits: (1) the primary circuit or collector circuit, in green, (2) the heating circuit, in red, and (3) the cooling circuit, in blue. The pipe's black sections close to the solar collector in the primary circuit correspond to flexible pipes that can be seen in Figure 1. The temperature control at the collector inlet (primary circuit) is done in two stages. First, the hot fluid at the collector outlet must be cooled, a process that is done by the heat exchanger IC1. The fluid is then precisely heated to match the required inlet temperature (set by the operator) through the heat exchanger IC2. The cooling circuit uses water at 10 °C that comes from an electric water chiller and the heating circuit uses hot water that comes from the 30 litre electric water heater. Each circuit has a circulation pump (B1, B2 and B3) and a manually regulated valve (VR1, VR2 and VR3). These valves are used to roughly set the flow in each circuit. The manually regulated valve VR4 is used to regulate the temperature of the fluid at the inlet of the IC1 heat exchanger, which mixes the hot return and the cold water at 10 °C. The flow rates in the three circuits are precisely regulated by electro-pneumatic valves (V51, V52 and V53), commanded by PID controllers (indicated by the dotted line). The entire control system was developed locally using a S7-1200 Siemens PLC. The diagram also indicates the location of the water temperature sensors (T_1, T_2, T_3, ϑ_i y ϑ_o), the ambient temperature sensor (ϑ_a), the global horizontal (G_h) and titled plane (G_t) irradiance sensors, the horizontal diffuse irradiance sensor (G_{dh}), the wind measurement (v) and the wind forcer (WG).

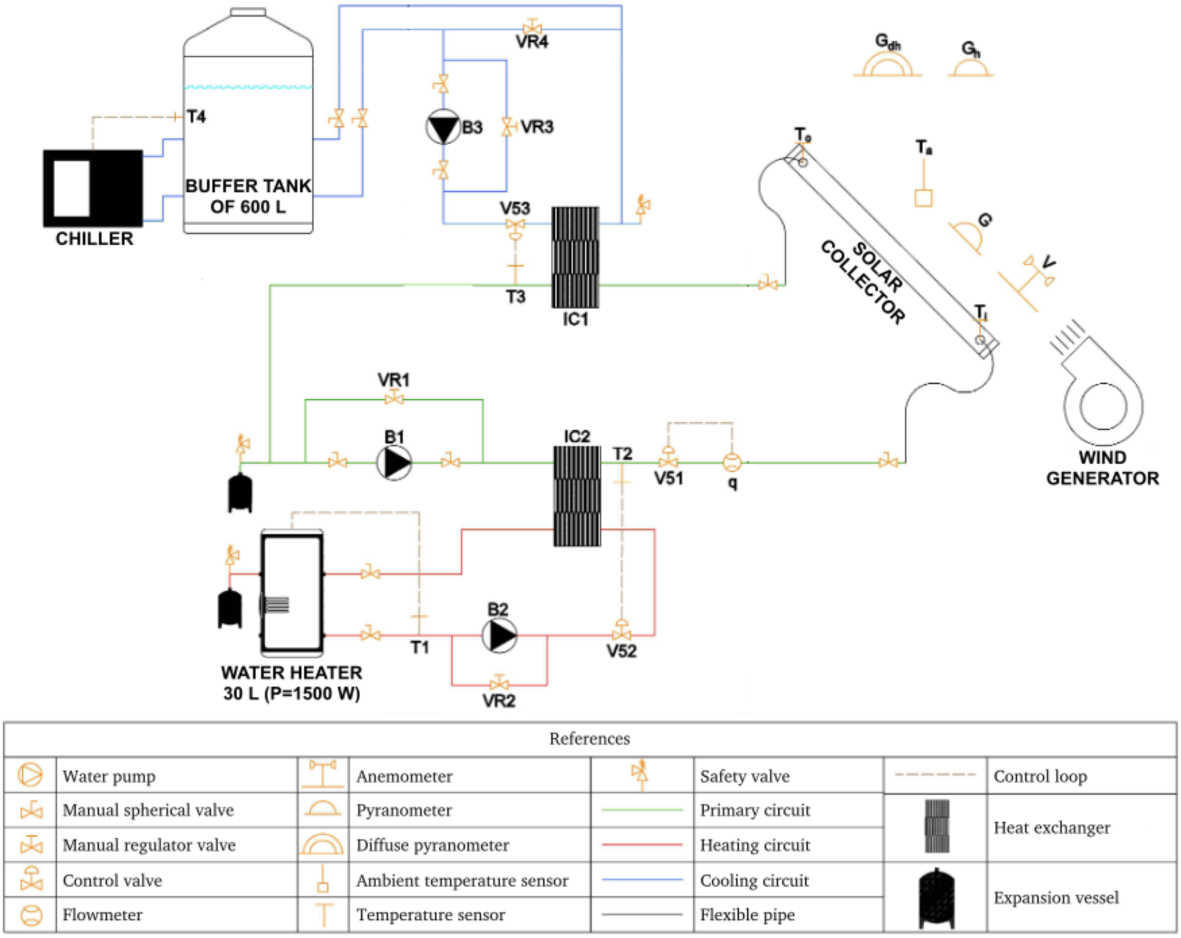

Figure 2: Thermo-hydraulic installation diagram.

To measure the temperature at the input and output of the collector (ϑ_i and ϑ_o), a 3 wire PT100 with 4-20 mA transmitters from Herten company were used. These sensors were calibrated at LES using a calibrated thermal bath and calibrated reference thermometers, reporting a standard uncertainty (P67, $k = 1$) of 0.02 °C. Ambient temperature (ϑ_a) was recorded with a Honeywell 2-wire PT1000 sensor also calibrated at LES with a standard uncertainty of 0.02 °C. The flow measurement (q) was performed with an Endress & Hauser electromagnetic flowmeter with a standard uncertainty of 0.5 % of the measurement. The wind speed parallel to the collector plane (v) was measured with an NGR cup anemometer with a standard uncertainty of 0.25 m/s. The global irradiance in the collector plane (G_t) was measured with a Kipp & Zonen CMP10 pyranometer. The global irradiance in the horizontal plane (G_h) was measured with a Kipp & Zonen CMP11 pyranometer and the diffuse irradiance in the horizontal plane (G_{dh}) with a Kipp & Zonen CMP6 pyranometer mounted with a shadow band from the same manufacturer. All the pyranometers used are spectrally flat (ISO-9060, 2018), being Class A for the global irradiance measurements (G_h and

G_t) and Class B for the diffuse irradiance measurement (G_{dh}). The diffuse irradiance measurement (with shadow band) was corrected with the expression provided by the manufacturer (Drummond, 1956). These pyranometers are calibrated annually at the LES according to the ISO-9847 (1992) standard against a Kipp & Zonen CMP22 secondary standard that is kept traceable to the world radiometric reference at the World Radiation Center in Davos, Switzerland. All measurements were recorded every 10 seconds using a Fischer Scientific DT85 datalogger. The G_{bt} direct irradiance in the collector plane was estimated from the G_h and G_{dh} with the following procedure. First, the direct normal irradiance (DNI, G_b) was calculated using the closure relation $G_h = G_b \cos\theta_z + G_{dh}$, where $\cos\theta_z$ is the cosine of the solar zenith angle. Then, the G_{bt} was calculated from the DNI, by multiplying with the cosine of the incident angle, θ.

3.2. Measured sequences

The tests were performed according to the ISO-9806 (2017) standard. During the tests, a wind speed of 3 m/s (spatial average) was imposed along the collector plane by using the air forcers shown in Figure 1. The fluid flow was set at 2.4 l/min and the tracker inclination angle was set at 45°. The azimuth was adjusted manually or automatically depending on the day type. The day types correspond to specific test sequences defined by the ISO-9806 (2017) standard and there are 4 different day types in total. Each of these sequences (day type) must have a duration of at least 3 hours and may be made up of several non-consecutive sub-sequences of at least 30 minutes each. The procedure and the purpose of each day type is described in the next paragraph. In all cases, before the measurement period, the collector was put through a conditioning period of 15 minutes at the corresponding test temperature. This period was not included in the models' parameter identification.

From the tests carried out, 16 different measurement sub-sequences were obtained; 11 of these sub-sequences were used to adjust the models and the remaining 5 were used for validation. The main characteristics of the training sub-sequences are shown in Table 1. This table shows the date and time of the test, the inlet temperature ϑ_i (average and maximum variability), the flow q (average and maximum variability), the average of the difference $\vartheta_m - \vartheta_a$, the diffuse fraction at the collector's plane $f_d^* = G_{dt}/G_t$ (range of variation) and the incident angle θ (range of variation). All the sequences meet the requirements for temperature and flow stability at the collector's inlet established in the ISO-9806 (2017) standard for the QDT methodology (variability less than ±1 °C and 2 %, respectively). The day type 1 sequence is made up of the sub-sequences $1a - 1e$. These series were obtained under clear sky conditions and during the tests an inlet temperature was set such that the mean temperature of the fluid was close to ambient temperature, that is, $\vartheta_m \simeq \vartheta_a$. These sequences (day type 1) are mostly used to determine $\eta_{0,b}$ and the IAM parameters. During sub-sequence $1a$, the solar tracker was configured so that it follows the position of the Sun in azimuth to obtain small incident angles ($\theta \leq 11.3°$). For sequences $1b - 1e$, the tracker was oriented North (fixed position) to obtain greater incident angles. Series $1b$ and $1c$ were measured before solar noon and series $1d$

and $1e$ after solar noon. The standard requires data measured before and after solar noon in approximately the same amount for large incident angles. The rest of the training sub-sequences (from $2a$ to $4b$) were obtained with azimuthal tracking to work in conditions close to those of normal incidence ($K_b \simeq 1$). This is not a requirement of the standard but it was done to achieve a greater decoupling of the independent variables and thus improve the parameter identification. Sub-sequences $2a$ and $2b$ were performed at an intermediate temperature and under variable sky conditions. The high variability of the diffuse fraction f_d^* in these sub-sequences accounts for this. These sub-sequences from day type 2 are useful to better identify the C and K_d parameters. The day type 3 and day type 4 sequences are mainly used to identify the thermal loss factors: a_1 and a_2. Sub-sequences $3a$ and $3b$ were performed at an intermediate temperature and in clear sky conditions. Sub-sequences $4a$ and $4b$ were performed at high temperature and in clear sky conditions.

Table 1: Description of the different measurement sub-sequences for model training.

Day type	Sub sec.	Date	Time	# data points	ϑ_i (°C)	q (l/min)	$\vartheta_m - \vartheta_a$ (°C)	f_d^*	θ (°)
1	1a	24/11	09:05-10:15	14	18.21(0.14)	2.39(0.7 %)	0.60	≤ 0.128	≤ 11.3
	1b	19/12	08:50-11:10	28	26.35(0.13)	2.39(0.9 %)	1.38	≤ 0.171	44.3-69.0
	1c	22/11	10:50-11:40	10	28.23(0.10)	2.39(0.7 %)	1.09	≤ 0.274	37.3-43.4
	1d	24/11	13:50-14:55	13	26.23(0.30)	2.39(0.7 %)	0.87	≤ 0.145	37.4-48.2
	1e	24/11	15:20-16:30	14	26.72(0.10)	2.39(0.9 %)	-0.32	≤ 0.195	52.2-65.0
2	2a	19/11	11:15-13:50	31	47.88(0.18)	2.39(0.7 %)	17.90	0.50-1.03	≤ 33.8
	2b	18/11	14:50-16:55	25	64.37(0.18)	2.39(1.0 %)	31.40	0.29-1.02	≤ 11.9
3	3a	17/11	15:05-16:40	19	49.74(0.19)	2.39(0.9 %)	20.10	≤ 0.117	≤ 10.4
	3b	28/11	09:35-11:35	24	65.29(0.12)	2.39(0.8 %)	41.74	≤ 0.105	≤ 27.5
4	4a	20/11	14:10-16:50	32	81.01(0.12)	2.39(1.0 %)	48.40	≤ 0.145	≤ 18.0
	4b	18/12	08:40-10:00	16	85.55(0.23)	2.39(0.8 %)	61.30	≤ 0.110	≤ 9.9

The main characteristics of the validation sub-sequences are shown in Table 2. These sub-sequences were obtained according to the day type 1 procedure (in clear sky conditions and with $\vartheta_m \simeq \vartheta_a$). This was done to reduce the effect of the parameters not linked to the IAM (K_d, a_1, a_2 and C) in the validation and thus focus on the effect that the different IAM models have on the collector performance (useful power). All validation sub-sequences were performed with the solar collector facing North (fixed position) to obtain large incident angles in the morning and in the afternoon. The $1f - 1h$ sub-sequences were performed before solar noon and the $1i - 1j$ sub-sequences after solar noon. As shown in Section 4, the relevant variations in IAM occur in the region of large incident angles ($\theta \gtrsim 40°$), for which the models are expected to provide a solution. For this reason, the focus is to evaluate the performance of the models in this range of angles.

Table 2: Description of the different measurement sequences for validation of the models.

Day type	Sub sec.	Date	Time	# data points	ϑ_i (°C)	q (l/min)	$\vartheta_m - \vartheta_a$ (°C)	f_d^*	θ (°)
	1f	6/12	08:25-09:45	16	24.06(0.73)	2.39(0.7 %)	2.6	≤ 0.206	58.3-71.3
	1g	6/12	9:50-10:55	13	26.36(0.62)	2.39(0.7 %)	3.3	≤ 0.132	44.2-68.3
1	1h	6/12	10:55-11:30	7	28.84(0.77)	2.39(0.9 %)	5.2	≤ 0.106	41.4-43.9
	1i	9/12	12:55-14:20	17	32.75(0.08)	2.39(0.8 %)	4.3	≤ 0.150	36.9-42.6
	1j	9/12	14:20-16:50	29	34.21(0.10)	2.39(0.7 %)	3.0	≤ 0.222	44.2-68.3

To obtain a day type 1 sequences, it is sufficient to measure the useful power from approximately normal incidence ($\theta \simeq 0°$) to angles greater than 60°. In this case, both the training sub-sequences and the validation sub-sequences were measured up to a 70° angle. useful power measurements in the presence of angles greater than 70° are associated with a high uncertainty, since in these conditions the collector works with a small temperature difference between its inlet and outlet due to the IAM adopting a very small value (close to zero). For the purposes of conducting annual performance simulations, it is considered acceptable to perform a linear approximation of the IAM in the range of 70° and 90°, with $K_b(90°) = 0$. The data series are available in http://les.edu.uy/RDpub/IAM_experimental_data.rar.

3.3. Performance evaluation

As mentioned in the previous section, the sub-sequences of Table 1 were used for model training, that is, to determine the characteristic parameters of each model. Then, with the parameters calculated in the previous step, the useful power produced by the collector was estimated for the sub-sequences of Table 2, in order to compare it with the experimental useful power. For these sub-sequences ($1f - 1j$), the Mean Bias Error (MBE) and the Root Mean Square Error (RMSE), in useful power per unit area, were calculated as shown in the following equations:

$$\text{MBE} = \frac{1}{N}\sum_{i=1}^{N}\left(\frac{\dot{Q}^*_{u,i}}{A_G} - \frac{\dot{Q}_{u,i}}{A_G}\right), \qquad \text{RMSE} = \sqrt{\frac{1}{N}\sum_{i=1}^{N}\left(\frac{\dot{Q}^*_{u,i}}{A_G} - \frac{\dot{Q}_{u,i}}{A_G}\right)^2}, \tag{11}$$

where N is the amount of data samples, $\dot{Q}^*_u$ is the estimated useful power (predicted with Eq. (1)) and $\dot{Q}_u$ is the experimental useful power. As a way of summarizing the information obtained by the MBE and the RMSE metrics into a single indicator, a third performance indicator was calculated, which consists of a combination of the previous ones (Combine Performance Indicator - CPI). This metric is shown in Eq. (12) and is similar to the one used in Gueymard (2012); Abal et al. (2017).

$$\text{CPI} = \frac{|\text{MBE}| + \text{RMSE}}{2}. \tag{12}$$

4. Results

4.1. Parameter identification

Table 3 shows the parameters value for the different considered models. These parameters were obtained from the experimental sub-sequences of Table 1 by linear or non linear regression as described in Subsection 2.3. Table 3 also shows the uncertainty of each parameter and the t-ratio. The t-ratio is the ratio between the value and its uncertainty, and is used to evaluate the statistical significance of a parameter. The parameter $K_b(80^{\circ} \rightarrow 90^{\circ})$ of model 4 and the parameter $K_b(80^{\circ})$ of model 5 were omitted from this table because the experimental measurements reach up to 70°. Furthermore, in the case of model 4, $K_b(0^{\circ} \rightarrow 10^{\circ}) = 1$ was imposed and for this reason this parameter is also omitted. For FPC and others the IAM is always less than unity (Duffie & Beckman, 1991). In the case of models 4 and 5, the experimental uncertainty can lead to the IAM adopting values slightly higher than this limit (Perers, 1997; Kong et al., 2012). To avoid this behavior, the physical constraint $K_b(\theta) \leq 1$ for all θ was imposed for these models.

It is common that different tests on the same collector arise to different a_1 and a_2 values. However, this differences tend to compensate between both parameters, that is, the higher the a_1 value, the lower the a_2 value and vice versa. This behavior can be seen in Fischer et al. (2004); García de Jalón et al. (2011); Osório & Carvalho (2014). For this reason it is not convenient to directly compare the value of these parameters separately. It is better to compare the combined effect through the global loss factor$a(\Delta\vartheta)$, which can be calculated as follows: $a(\Delta\vartheta) = a_1 + a_2\Delta\vartheta$, where the temperature difference is $\Delta\vartheta = \vartheta_m - \vartheta_a$. It is usual to use the loss factor combined to a temperature difference of 50 °C for this kind of collector. The value of this parameter, $a(50\,^{\circ}\mathrm{C}) = a_{50}$, is also shown in Table 3. This parameter was the one used in the test laboratory inter-comparison mentioned in Subsection 3.1 (Fischer, 2020).

The ISO-9806 (2017) standard establishes that a parameter has been correctly identified (statistically significant) if the t-ratio is greater than 3. Table 3 shows that in all cases a t-ratio greater than this value was obtained except for the case of the b_1 parameter of the Kalogirou model, where a value of 1.5 was obtained. According to the standard, this suggests that this parameter can be omitted from the model in this case, and that it is possible for this collector to use a model that consists only of the second-order term without significant loss of performance. Table 3 particularly highlights the high t-ratio of the parameters associated with IAM models 4 and 5, being in all cases higher than those of models 1, 2 and 3 (n, b_0, b_1 y b_2). It is observed that the value of the parameters $\eta_{0,b}$, K_d, a_{50} and C/A_G, common to the 5 models, are very close to each other, with differences of less than $\pm 3\,\%$.

Table 3: Value, uncertainty and t-ratio of the characteristic parameters of each of the considered models. Units for the parameters are indicated in the nomenclature list at the end of the article.

Model 1 ISO-9806 (2017)				Model 2 Souka & Safwat (1966)				Model 3 Kalogirou (2004)			
param.	value	uncert.	t-ratio	param.	value	uncert.	t-ratio	param.	value	uncert.	t-ratio
$\eta_{0,b}$	0.721	0.001	1030	$\eta_{0,b}$	0.725	0.001	515	$\eta_{0,b}$	0.718	0.001	665
K_d	0.971	0.003	303	K_d	0.973	0.006	163	K_d	0.967	0.005	201
n	3.811	0.036	107	b_0	0.121	0.005	26	b_1	0.0121	0.0082	$\underline{1.5}$
a_1	4.155	0.060	69	a_1	4.311	0.144	38	b_2	0.106	0.007	15
a_2	0.084	0.0010	8	a_2	0.0074	0.0020	4	a_1	4.051	0.081	50
a_{50}	4.575	0.078	58	a_{50}	4.681	0.151	31	a_2	0.0101	0.0052	8
C/A_G	10919	304	36	C/A_G	11029	581	19	a_{50}	4.556	0.272	43
								C/A_G	10730	406	27

Model 4 Perers (1997)				Model 5 (this work)			
param.	value	uncert.	t-ratio	param.	value	uncert.	t-ratio
$\eta_{0,b}$	0.714	0.001	562	$\eta_{0,b}$	0.716	0.001	581
K_d	0.976	0.005	187	K_d	0.975	0.004	229
$K_b(10° \to 20°)$	1.000	0.003	401	$K_b(10°)$	1.000	0.003	391
$K_b(20° \to 30°)$	1.000	0.004	293	$K_b(20°)$	1.000	0.003	364
$K_b(30° \to 40°)$	0.994	0.005	221	$K_b(30°)$	1.000	0.006	158
$K_b(40° \to 50°)$	0.990	0.003	287	$K_b(40°)$	0.998	0.003	331
$K_b(50° \to 60°)$	0.921	0.004	234	$K_b(50°)$	0.962	0.003	276
$K_b(60° \to 70°)$	0.823	0.006	137	$K_b(60°)$	0.882	0.004	202
a_1	4.249	0.108	40	$K_b(70°)$	0.714	0.012	62
a_2	0.0070	0.0018	4	a_1	4.210	0.076	55
a_{50}	4.599	0.140	33	a_2	0.0076	0.0013	6
C/A_G	10967	472	24	a_{50}	4.590	0.100	46
				C/A_G	10791	338	33

To compare the different IAM models with each other, K_b was calculated as a function of θ in the range $0° - 70°$ for each model. The resulting models are shown in Figure 3. It is evident that the collector used has a very good optical performance since K_b is close to unity in the range of 0° to 40°. In this range ($0° - 40°$), the different IAM models have values that are very similar to each other, with the maximum difference between them being less than 3 %. In contrast, K_b changes more abruptly in the range between 40° and 70°, where the largest discrepancies are observed between the models. The largest difference occurs at node 70°

and corresponds to 33 %.

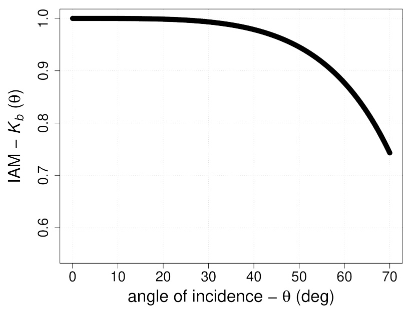

(a) Model 1, ISO-9806 (2017).

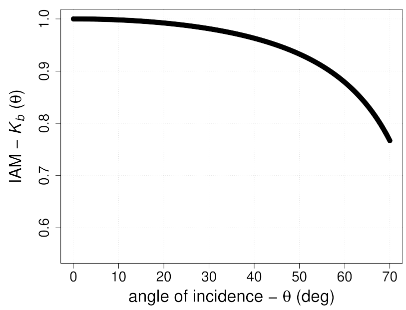

(b) Model 2, Souka & Safwat (1966).

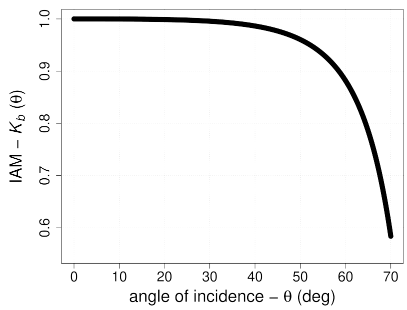

(c) Model 3, Kalogirou (2004).

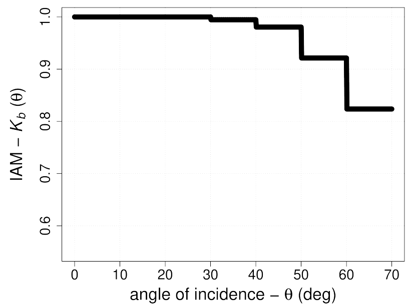

(d) Model 4 Perers (1997).

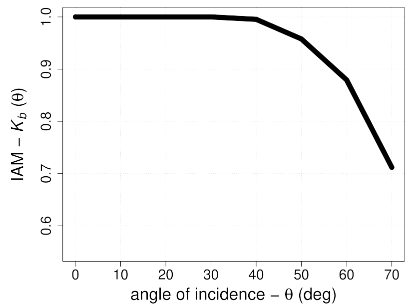

(e) Model 5, (this work).

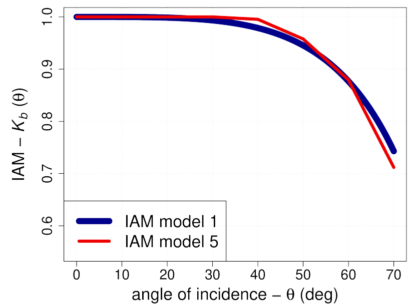

(f) Comparison between models 1 and 5.

Figure 3: $K_b(\theta)$ graph as a function of the θ incident angle for each model. Figure (f) shows the comparison between the novel model and the one suggested by the ISO-9806 (2017); model 1 (blue) and 5 (red). The parameters of the corresponding models are those of Table 3. The data for these plots can be accessed in http://les.edu.uy/RDpub/IAM_Fig3_data.zip.

4.2. Performance of IAM models

Table 4 shows the performance indicators (MBE, RMSE and CPI) for each model, using the sub-sequences $1f-1g$ for their validation (see Table 2). The indicators are calculated for the θ interval between 40° and 70°, since this is the range where the higher K_b variations occur. Indicators are also provided for the $40° - 50°$, $50° - 60°$ and $60° - 70°$ sub-intervals. The models were classified according to the global performance metric (CPI) in each interval (ranking: from 1 to 5). At the end of this table, the amount of data in each sub-interval is presented and it can be seen that the data is approximately uniformly distributed (about one third of the data is in each sub-interval). Figure 4 shows the scatter plots between the estimated useful power vs. experimental useful power (black dots), both per unit area, for each IAM model. The perfect agreement line $x = y$ (in red) is included in the graphs to help interpret the results. Note that higher values of useful power per unit area are associated with lower incident angles and vice versa.

The model 1 presents a CPI of 6.6 W/m^2 in the global $40° - 70°$ range, thus ranking third in terms of performance. When observing the MBE discriminated by intervals, this model underestimates the experimental data (MBE < 0) in the $40° - 50°$ and $50° - 60°$ sub-intervals, and overestimates it (MBE > 0) in the

Table 4: Performance of the different models for the $1f - 1j$ sequences.

Model	Indicator	Incident angle θ			
		$40° - 50°$	$50° - 60°$	$60° - 70°$	$40° - 70°$
Model 1	MBE (W/m^2)	-8.7	-7.1	2.5	**-4.7**
ISO-9806 (2017)	RMSE (W/m^2)	9.8	8.5	7.0	**8.6**
	CPI (W/m^2)	9.2	7.8	4.7	**6.6**
	Rank	4	3	1	**3**
Model 2	MBE (W/m^2)	-13.4	-7.9	7.3	**-5.3**
Souka & Safwat (1966)	RMSE (W/m^2)	14.2	9.8	10.4	**11.8**
	CPI (W/m^2)	13.8	8.9	8.9	**8.5**
	Rank	5	4	4	**5**
Model 3	MBE (W/m^2)	-4.9	-2.9	-8.3	**-5.3**
Kalogirou (2004)	RMSE (W/m^2)	6.6	5.0	10.4	**7.6**
	CPI (W/m^2)	5.7	3.9	9.4	**6.5**
	Rank	3	1	5	**2**
Model 4	MBE (W/m^2)	-3.5	-8.6	-0.5	**-4.2**
Perers (1997)	RMSE (W/m^2)	7.1	13.8	15.7	**12.5**
	CPI (W/m^2)	5.3	11.2	8.1	**8.3**
	Rank	1	5	3	**4**
Model 5	MBE (W/m^2)	-4.7	-6.9	-3.9	**-5.2**
(this work)	RMSE (W/m^2)	6.5	7.8	6.6	**7.0**
	CPI (W/m^2)	5.6	7.3	5.2	**6.1**
	Rank	2	2	2	**1**
amount of data per bin		23(37.7 %)	19(31.1 %)	19(31.1 %)	**61(100%)**

$60° - 70°$ sub-interval. This behavior can be seen in Figure 4a. Although this model is in the third place in the global ranking, close to the second one, in the $40° - 50°$ sub-interval it presents a poor performance (rank 4). Model 2 presents a CPI of $8.5\,W/m^2$ in the $40° - 70°$ range, thus ranking last in terms of performance. When observing the MBE discriminated by intervals, this model present a similar bias behavior that model 1 as it underestimates the experimental data in the $40° - 50°$ and $50° - 60°$ sub-intervals, and overestimates in the $60° - 70°$ sub-interval, but in a greater extent. The model 2 not only presents the worst overall performance, but also provides a weak performance in discriminated sub-intervals, ranking almost last for all of them. The model 3 presents a CPI of $6.5\,W/m^2$ in the $40° - 70°$ range and ranks second. When looking at the indicators discriminated by sub-intervals, a good performance is observed in the first two ($40° - 50°$ and

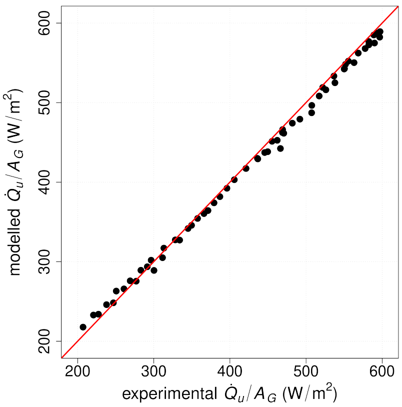

(a) Model 1, ISO-9806 (2017).

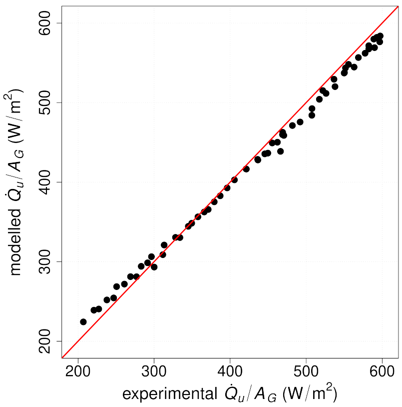

(b) Model 2, Souka & Safwat (1966).

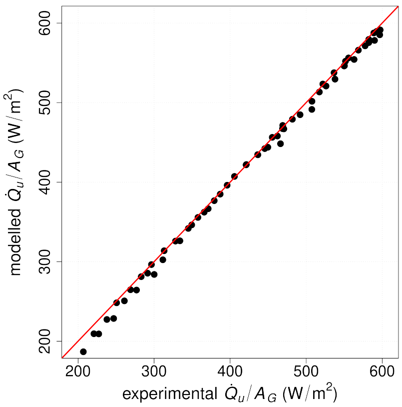

(c) Model 3, Kalogirou (2004).

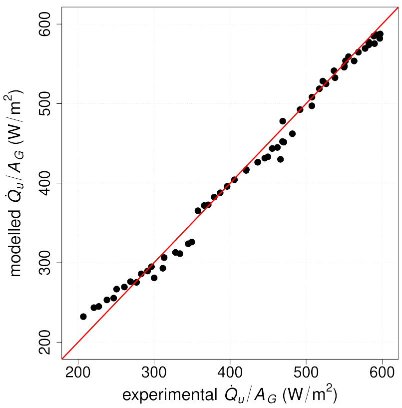

(d) Model 4 Perers (1997).

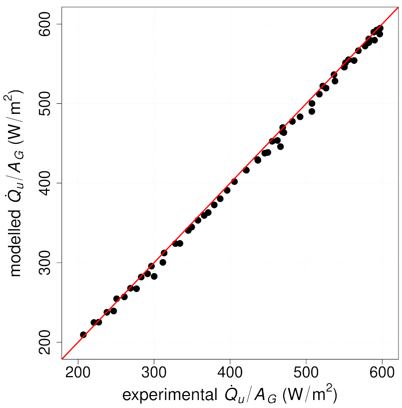

(e) Model 5 (this work).

Figure 4: Scatter plots of estimated vs. experimental useful power (points), both per unit area. The perfect agreement line is shown in red to help interpret the data. The data for this plot can be accessed in http://les.edu.uy/RDpub/Qu_Fig4_data.zip.

$50° - 60°$) but a poor performance is observed in the last. If the b_1 parameter of this model is set to zero and the parameter identification is performed again, omitting the variable associated with this parameter, the performance of the model improves a little in the first sub-interval, but the overall performance ($40° - 70°$ range) does not change significantly, retaining its position in the global ranking (second place). This is in agreement with the t-ratio observed for the b_1 parameter in Table 3. The b_1 parameter of this model is, in effect, removable for this collector, leaving a second order model in the variable $(1/\cos\theta - 1)$ that has a better performance than model 2. The model 4 presents a CPI of $8.3\,\mathrm{W/m^2}$ in the $40° - 70°$ range and is located in fourth place, very close to model 2. This model presents a very good performance in the first interval but it downgrades significantly in the following ones. In Figure 4d the effect of the discontinuities in the model (typical of a constant piecewise function) can be observed at 50° and 60° angles. This same figure shows the reason why this model has a high RMSE and a low MBE. In all the model's sub-intervals there is a region where the model underestimates and another region where the model overestimates. These differences tend to compensate for the MBE, but the squared differences are not compensated, resulting in a high RMSE value. Finally, the model 5 presents a CPI of $6.1\,\mathrm{W/m^2}$ in the $40° - 70°$ range and is ranked in the first place, showing a better performance in comparison with models 1 and 3 and significantly better in comparison to models 2 and 4 (CPI is reduced by 6 % and 27 % in respect to the former and latter ones). The model 5 has also a very good performance in all considered sub-ranges of incident angles, ranked as 2 in each sub-interval, showing an homogeneous behavior. Figure 4e provides evidence of this good performance. It is also highlighted that in the last interval ($60° - 70°$), the new model has a significantly lower CPI than the other linear models (models 2, 3 and 4), with a reduction of 35 %. In this last interval the performance of the novel model is only improved by the non linear model 1. However, in the first sub-interval ($40° - 50°$), model 5 outperforms importantly model 1, with a CPI reduction of 39 %.

In sum, three groups of models can be roughly distinguished: (i) the models 2 and 4 with a CPI of $\simeq 8.5\,\mathrm{W/m^2}$, (ii) the models 1 and 3, with a CPI of $\simeq 6.5\,\mathrm{W/m^2}$, and (iii) the proposed model, which achieves the lowest CPI of $\simeq 6.0\,\mathrm{W/m^2}$. The models in the (i) and (ii) categories may have a good performance in one sub-interval but typically underperform in at least one them due to a worse modelling of the overall IAM behavior. On the contrary, model 5 has not this drawback, being its performance homogeneous across the $40° - 70°$ incident angles range. Also, being linear, its implementation is simple, therefore it is also the best choice considering the accuracy-simplicity tradeoff.

If a smaller angular step is used for models 4 and 5, for example of 5° instead of 10°, the conclusions do not change. The overall performance of model 4 improves, but fails to exceed that of model 5 with an angular step of 10°. Furthermore, model 4 with 5° resolution continues to show large RMSE values in the range ($60° - 70°$). Ideally, if the angular resolution is lowered enough, the performance of models 4 and 5 should converge to the same value. However, reducing the angular step in practice presents difficulties because obtaining an adequate amount of data for each interval depends on the Sun's apparent path at the test location and the averaging time of the data. On the other hand, reducing the angular resolution requires the addition of more parameters (associated with more independent variables) in the piecewise linear regression models, which makes the parameter identification procedure more complex and more experimental data are required. A resolution of 10° for model 5 allows the IAM to be adequately characterized with a low level of error, it is feasible in practice and it allows keeping the number of independent variables limited.

4.3. Sensitivity to measured data

In this section, the sensitivity of the IAM models to the variability of the input data is evaluated, that is, how much the parameters of the models vary when considering different training sets. For this, by using the sub-sequences of Table 1 and 2 together, 8 different data sets were defined, from A to H. Table 5 shows the composition of the different data sets, indicating the sub-sequences from Table 1 and 2 that constitute each set. All the sets in this table are composed of the same data sub-sequences for day type 2, day type 3 and day type 4, differing only in the sequences for day type 1. One of the requirements of ISO-9806 (2017) is that data sets must contain measurements before and after solar noon (balanced data set). In this sense, the sets from A to D are sets that meet this requirement. Sets E to H do not meet this requirement; sets E and F have measurements only before solar noon and sets G and H only after. All sets include the sub-sequence 1a, which is not relevant if it was taken before or after solar noon because azimuthal tracking was carried out during this sub-sequence. This sub-sequence is important to correctly determine the $\eta_{o,b}$ parameter, since it comprises small incident angles, so it was included in all sets.

Table 5: Composition of the different data sets for sensitivity analysis.

Data set name	Sequences day type 1	Sequences day type 2, 3 and 4	Balanced data set	# data points
A	$1a, 1b, 1c, 1d, 1e$	$2a, 2b, 3a, 3b, 4a, 4b$	yes	226
B	$1a, 1b, 1c, 1i, 1j$	$2a, 2b, 3a, 3b, 4a, 4b$	yes	245
C	$1a, 1f, 1g, 1h, 1d, 1e$	$2a, 2b, 3a, 3b, 4a, 4b$	yes	224
D	$1a, 1f, 1g, 1h, 1i, 1j$	$2a, 2b, 3a, 3b, 4a, 4b$	yes	243
E	$1a, 1b, 1c$	$2a, 2b, 3a, 3b, 4a, 4b$	no	199
F	$1a, 1f, 1g, 1h$	$2a, 2b, 3a, 3b, 4a, 4b$	no	197
G	$1a, 1d, 1e$	$2a, 2b, 3a, 3b, 4a, 4b$	no	188
H	$1a, 1i, 1j$	$2a, 2b, 3a, 3b, 4a, 4b$	no	207

The purpose of the sets from E to H is to evaluate the relevance of the balanced set requirement in the standard when using the different IAM models. The elimination of this requirement allows the reduction of the testing time. The last column of Table 5 indicates the amount of data that each data set contains. We shall recall that each point corresponds to an average in 5 minutes. The ABCD sets have 235 points on average, which is equivalent to ∼19.5 hours of testing, while the EFGH sequences have 198 data points on average, which is equivalent to ∼16.5 hours of testing and represents a reduction of 3 hours within testing (∼15%) with respect to the duration of the ABCD sets.

The sensitivity analysis was done as follows. First, the characteristic parameters for each of the data sets in Table 5 (from A to H) were determined. Then, for each parameter the average of the ABCD sets was determined. These averages were taken as the reference values for the parameters, as the sets from A to D comply with the standard. The variability of each parameter was calculated, for the ABCD and EFGH groups, as the maximum between: (1) the maximum value found in the sets minus the reference value and (2) the reference value minus the minimum value found in the sets. The relative variability was calculated as the found variability divided by the reference value and expressed as a percentage. Table 6 shows the results of this analysis for the 4 models. In the last two rows, for each model, the average and the standard deviation of the relative variability of all the parameters is presented, excluding for this calculation the a_{50}

parameter, which is not a parameter obtained directly from the models.

Table 6: Sensitivity analysis results. Units for the parameters are indicated in the nomenclature list at the end of the article.

Model 1 ISO-9806 (2017)				Model 2 Souka & Safwat (1966)				Model 3 Kalogirou (2004)			
param.	mean ABCD	var. ABCD	var. EFGH	param.	mean ABCD	var. ABCD	var. EFGH	param.	mean ABCD	var. ABCD	var. EFGH
$\eta_{0,b}$	0.721	0.1 %	0.3 %	$\eta_{0,b}$	0.726	0.1 %	0.6 %	$\eta_{0,b}$	0.718	0.0 %	0.1 %
K_d	0.967	0.4 %	0.3 %	K_d	0.967	0.6 %	0.7 %	K_d	0.964	0.4 %	0.3 %
n	3.811	2.6 %	4.4 %	b_0	0.117	3.6 %	13.6 %	b_1	0.009	49 %	281 %
a_1	4.122	1.5 %	1.9 %	a_1	4.226	2.1 %	5.1 %	b_2	0.097	12 %	37.4 %
a_2	0.0097	13.0 %	9.7 %	a_2	0.0092	19.1 %	27.5 %	a_1	3.987	2.0 %	0.9 %
a_{50}	4.605	0.6 %	0.8 %	a_{50}	4.685	0.5 %	2.2 %	a_2	0.0110	12.1 %	7.1 %
C/A_G	10602	4.0 %	2.7 %	C/A_G	10648	4.2 %	4.1 %	a_{50}	4.546	0.3 %	0.4 %
mean var.		3.2 %	2.9 %	mean var.		4.4 %	7.7 %	C/A_G	10615	3.5 %	2.9 %
std var.		4.5 %	3.4 %	std var.		6.8 %	9.8 %	mean var.		9.8 %	41.3 %
								std var.		16.5 %	97.7 %

Model 4 Perers (1997)				Model 5 (this work)			
param.	mean ABCD	var. ABCD	var. EFGH	param.	mean ABCD	var. ABCD	var. EFGH
$\eta_{0,b}$	0.716	0.3 %	0.2 %	$\eta_{0,b}$	0.715	0.0 %	0.0 %
K_d	0.973	0.3 %	1.0 %	K_d	0.975	0.2 %	0.3 %
$K_b(10° \to 20°)$	1.008	0.1 %	0.1 %	$K_b(10°)$	1.004	0.1 %	0.1 %
$K_b(20° \to 30°)$	1.013	0.1 %	0.1 %	$K_b(20°)$	1.016	0.1 %	0.1 %
$K_b(30° \to 40°)$	0.997	0.4 %	8.5 %	$K_b(30°)$	1.012	0.3 %	0.4 %
$K_b(40° \to 50°)$	0.985	0.5 %	0.7 %	$K_b(40°)$	0.999	0.3 %	0.8 %
$K_b(50° \to 60°)$	0.933	1.3 %	1.8 %	$K_b(50°)$	0.971	0.9 %	1.2 %
$K_b(60° \to 70°)$	0.828	1.3 %	1.6 %	$K_b(60°)$	0.891	1.1 %	1.7 %
a_1	4.153	2.5 %	3.0 %	$K_b(70°)$	0.717	2.3 %	3.2 %
a_2	0.0086	20.1 %	23.0 %	a_1	4.139	2.9 %	1.9 %
a_{50}	4.583	0.4 %	0.5 %	a_2	0.0086	15.8 %	12.3 %
C/A_G	10626	4.8 %	3.3 %	a_{50}	4.566	1.2 %	0.5 %
mean var.		2.7 %	3.7 %	C/A_G	10675	2.9 %	2.7 %
std var.		5.7 %	6.5 %	mean var.		2.2 %	1.9 %
				std var.		4.2 %	3.3 %

When the ABCD data sets are considered, it is observed that models 1, 2, 4 and 5 show low variability in all parameters except for a_2. In the case of model 3, a low variability is observed in the parameters $\eta_{0,b}$, K_d, a_1 and C/A_G, but a high variability is observed in the parameters a_2, b_1 and b_2. It should be noted that although in all cases there is a high variability of the a_2 parameter, this variability tends to be compensated by that of a_1 and ultimately the global loss coefficient, a_{50}, varies little.

When the EFGH data sets are considered, a behavior similar to the previous one is observed but there is a notable increase in the variability of the following parameters: b_0 (model 2), b_1 and b_2 (model 3), and $K_b(30^\circ \to 40^\circ)$ (model 4). In the case of the b_1 parameter, which presents a notorious high variability, it happens that some sets (FGH) result in a negative value for it, and the sign change with respect to the reference value (average of ABCD, $b_1 > 0$) and its small value causes the high relative variability. Even if the parameter b_1 is not taken into account, that is, if the variable associated with this parameter is omitted in the parameter identification, the variability of b_2 continues to be large in both cases, whether the ABCD or EFGH sets are considered. In the case of the $K_b(30^\circ \to 40^\circ)$ parameter, the dynamic effects are not being compensated correctly as the determination of this parameter is mainly determined through the $2a$ sub-sequence (see Table 1), which belongs to the day type 2 and is associated with high sky variability (and thus high variability of $d\vartheta_m/dt$). In model 1, an increase in the variability of n parameter is observed. Finally, in model 5, no significant increase in variability is observed in any of the parameters when considering the ABCD sets against the EFGH sets. In average terms, a general increase in the variability of the parameters is observed in linear models 2, 3 and 4 when moving from one set to another, being the Perers model the least affected of these 3 (see last rows of Table 6). In the case of model 1 and 5, the average variability even decreases slightly when moving from a balanced set to an unbalanced one, being the models less affected by a change in the adjustment sequences.

In short, it is seen that models 1 and 5 are the most reliable to use as they are less sensitive to variations in the input data. In addition, this models can be implemented by using data sets containing measurements only before or after solar noon. In fact, the novel proposal shows the lowest variability of the models tested here and, being of $\simeq 2\%$, it further enables to reduce the testing times by considering only morning or afternoon data series. The model 3 is the most sensitive and it is not recommended to use it with unbalanced data sets (morning or afternoon data only). The model 2 also shows the same limitation, in a lesser extent, but it is also not recommended in this sense. The model 4, although a good overall variability is observed, it has an important increased variability in one of its main parameters. To summarize, the reliability ranking against variations in the input data of the analyzed models is, from highest to lowest: model 5, model 1, model 4, model 2 and model 3.

5. Conclusions

In this work, a new linear IAM model was proposed to be used for QDT of flat plate solar collectors under the ISO-9806 (2017) standard. The performance of this model was evaluated and compared with that of four other models available in the literature. This include two linear models widely-used for QDT (Souka & Safwat, 1966; Perers, 1997), another linear model not tested yet for QDT (Kalogirou, 2004) and the non linear model suggested by the ISO-9806 (2017) standard for SST. For the comparison, a data set was used to train the models and an independent data set was used to evaluate them. The tests and measurements were performed according to ISO-9806 (2017) standard. The comparison showed that the proposed model (with a resolution of 10°) presents a very good performance in the entire range of incidence angles, outperforming in overall all the others models (even if the Perers model is used with an increased angular resolution of 5°). The proposed model also has a balanced behavior in all incident angles sub-intervals, with homogeneous metrics across them, ranking second in each one. This is not observed for the other models, that typically fail to represent at least one sub-range. This is a remarkable property of the novel model, which describes better the IAM behavior in its whole range without misrepresenting, in particular, large incident angles in where the IAM variations are greater. We also think that this property makes the model a good choice to be used in the testing of solar thermal collectors with more complex IAM behavior, such as vacuum tube collectors, which is part of our current work. The proposed model, being linear, is simple to employ for QDT, thus can be implemented, for instance, in a standard spreadsheet in the same way as the other widely-used linear models, but with higher accuracy.

On the other hand, the variability of the models' parameters was analyzed against the variation of the input data set (sensitivity analysis). This analysis showed that the proposed model is the most reliable as the parameters of this model are less sensitive to variations in the input data. It was shown that the proposed model can be used with unbalanced data sets (not symmetric with respect to solar noon) without loss of performance in the determination of its parameters, that is, by using sets only containing data obtained in the morning or in the afternoon. This property allows to reduce the time of the tests. Further case studies of this property are required, accounting for different climates, to give this observation a more general scope.

The use of the Kalogirou (2004) and Ambrosetti (ISO-9806, 2017) models have not been reported yet for the standard QDT methodology and were included in this work. Both models showed a fair overall performance in the $40° - 70°$ range, and are indeed good choices for QDT. However, both of them present difficulties in representing at least one of the incident angles sub-ranges. The sensitivity analysis showed that Kalogirou model is sensitive to the variability of the training data and that its utilization with unbalanced data sets is not recommended. So, it is possible to use this model for QDT, provided that this observation is taken into account.

Acknowledgments

The authors would like to thank the Ministerio de Industria, Energía y Minería (MIEM, Uruguay), especially its Dirección Nacional de Energía (DNE), the Fideicomiso Uruguayo de Ahorro y Eficiencia Energética (Fudaee, Uruguay) and the Corporación Nacional para el Desarrollo (CND, Uruguay), for having provided financial and logistical support for the development of the BECS facility and for having promoted this project with local capacities. The authors are also grateful to the PTB of Germany for promoting and financing the inter-laboratory on efficiency test of solar collectors, which has given us technical certainty about our local testing capabilities.

Nomenclature

Symbol	Definition	Units
A_G	gross collector area	m^2
a_1	first order thermal loss factor	$\mathrm{W/m^2K}$
a_2	second order thermal loss factor	$\mathrm{W/m^2K^2}$
a_{50}	global thermal loss factor at $(\vartheta_m - \vartheta_a) = 50\,°\mathrm{C}$	$\mathrm{W/m^2K}$
b_0	adjustable parameter of the Souka & Safwat	-
b_1, b_2	adjustable parameters of the Kalogirou	-
C	collector thermal capacity	$\mathrm{J\,K^{-1}}$
CPC	compound parabolic concentrators	-
CPI	combine performance indicator	$\mathrm{W/m^2}$
DNI	direct normal irradiance	$\mathrm{W/m^2}$
f_d^*	diffuse fraction in the plane of the collector	-
FPC	flat plate collector	-
G_h	global solar irradiance at an horizontal plane	$\mathrm{W/m^2}$
G_b	direct normal irradiance	$\mathrm{W/m^2}$
G_{dh}	diffuse solar irradiance at an horizontal plane	$\mathrm{W/m^2}$
G_t	global solar irradiance at the collector plane	$\mathrm{W/m^2}$
G_{bt}	direct solar irradiance at the collector plane	$\mathrm{W/m^2}$
G_{dt}	diffuse solar irradiance at the collector plane	$\mathrm{W/m^2}$
IAM	incident angle modifier	-
K_b	incidence angle modifier for direct solar irradiance	-
K_d	incidence angle modifier for diffuse solar irradiance	-
MBE	mean bias error	$\mathrm{W/m^2}$
MLR	multi-linear regression	-
n	adjustable parameter of the ISO-9806	-
$\dot{Q}_u$	useful power produced by the collector	W
QDT	quasi-dynamic testing	-
SST	steady state testing	-
RMSE	root mean square error	$\mathrm{W/m^2}$
ϑ_i	fluid temperature at the collector inlet	°C
ϑ_o	fluid temperature at the collector outlet	°C
ϑ_m	mean temperature of the fluid passing through the collector	°C
ϑ_a	ambient air temperature	°C
$\eta_{0,b}$	collector peak efficiency referred to direct solar irradiance	-
θ	incidence angle of direct solar irradiance in the collector plane	deg
θ_z	solar zenith angle	deg

References

Abal, G., Aicardi, D., Alonso Suárez, R., & Laguarda, A. (2017). Performance of empirical models for diffuse fraction in uruguay. *Solar Energy*, *141*, 166 – 181. URL: http://www.sciencedirect.com/science/article/pii/S0038092X1630562X. doi:https://doi.org/10.1016/j.solener.2016.11.030.

Drummond, A. J. (1956). On the measurement of sky radiation. *Archiv für Meteorologie, Geophysik und Bioklimatologie, Serie B*, *7*, 413 – 436. URL: https://link.springer.com/article/10.1007%2FBF02242969. doi:https://doi.org/10.1007/BF02242969.

Duffie, J. A., & Beckman, W. A. (1991). *Solar engineering of thermal processes*. John Wiley & Sons.

Eck, M., Hirsch, T., Feldhoff, J., Kretschmann, D., Dersch, J., Morales, A. G., Gonzalez-Martinez, L., Bachelier, C., Platzer, W., Riffelmann, K.-J., & Wagner, M. (2014). Guidelines for csp yield analysis – optical losses of line focusing systems; definitions, sensitivity analysis and modeling approaches. *Energy Procedia*, *49*, 1318 – 1327. URL: http://www.sciencedirect.com/science/article/pii/S1876610214005955. doi:https://doi.org/10.1016/j.egypro.2014.03.141. Proceedings of the SolarPACES 2013 International Conference.

Fischer, S. (2020). *Quality Infrastructure for Energy Efficiency and Renewable Energy in Latin America and the Caribbean, Report # 95309*. Report Intituto Metrológico Aleman - PTB. URL: http://les.edu.uy/report/Expert_Report-RR-Test_R1.pdf.

Fischer, S., Heidemann, W., Müller-Steinhagen, H., Perers, B., Bergquist, P., & Hellström, B. (2004). Collector test method under quasi-dynamic conditions according to the european standard en 12975-2. *Solar Energy*, *76*, 117 – 123. URL: http://www.sciencedirect.com/science/article/pii/S0038092X03002901. doi:https://doi.org/10.1016/j.solener.2003.07.021.

Gueymard, C. A. (2012). Clear-sky irradiance predictions for solar resource mapping and large-scale applications: Improved validation methodology and detailed performance analysis of 18 broadband radiative models. *Solar Energy*, *86*, 2145 – 2169. URL: http://www.sciencedirect.com/science/article/pii/S0038092X11004221. doi:https://doi.org/10.1016/j.solener.2011.11.011. Progress in Solar Energy 3.

ISO-9060 (2018). *Solar energy — Specification and classification of instruments for measuring hemispherical solar and direct solar radiation*. Standard International Organization of Standarization Switzerland.

ISO-9806 (2017). *Solar Energy – Solar thermal collectors – Test methods*. Standard International Organization of Standarization Switzerland.

ISO-9847 (1992). *Solar Energy – Calibration of field pyranometers by comparison to a reference pyranometer*. Standard International Organization of Standarization Switzerland.

García de Jalón, A., Sallaberry, F., Olano, X., , Mateu, E., Astiz, R., Ezcurra, M., & Ramíres, L. (2011). Comprarison of thermal efficiency curves of solar collectors tested in outdoor conditions. In *Proceedings of ISES World Congress 2011*. URL: http://proceedings.ises.org/paper/eurosun2010/eurosun2010-0269-Sallaberry.pdf.

Kalogirou, S. A. (2004). Solar thermal collectors and applications. *Progress in Energy and Combustion Science*, *30*, 231 – 295. URL: http://www.sciencedirect.com/science/article/pii/S0360128504000103. doi:https://doi.org/10.1016/j.pecs.2004.02.001.

Kong, W., Wang, Z., Fan, J., Bacher, P., Perers, B., Chen, Z., & Furbo, S. (2012). An improved dynamic test method for solar collectors. *Solar Energy*, *86*, 1838 – 1848. URL: http://www.sciencedirect.com/science/article/pii/S0038092X12001077. doi:https://doi.org/10.1016/j.solener.2012.03.002.

Kratzenberg, M., Beyer, H., & Colle, S. (2006). Uncertainty calculation applied to different regression methods in the quasi-dynamic collector test. *Solar Energy*, *80*, 1453 – 1462. URL: http://www.sciencedirect.com/science/article/pii/S0038092X06000880. doi:https://doi.org/10.1016/j.solener.2006.03.010.

McIntire, W. R. (1982). Factored approximations for biaxial incident angle modifiers. *Solar Energy*, *29*, 315 – 322. URL: http://www.sciencedirect.com/science/article/pii/0038092X82902468. doi:https://doi.org/10.1016/0038-092X(82)90246-8.

Muschaweck, J., & Spirkl, W. (1993). Dynamic solar collector performance testing. *Solar Energy Materials and Solar Cells*, *30*, 95 – 105. URL: http://www.sciencedirect.com/science/article/pii/092702489390011Q. doi:https://doi.org/10.1016/0927-0248(93)90011-Q.

Osório, T., & Carvalho, M. J. (2014). Testing of solar thermal collectors under transient conditions. *Solar Energy*, *104*, 71 – 81. URL: http://www.sciencedirect.com/science/article/pii/S0038092X14000851. doi:https://doi.org/10.1016/j.solener.2014.01.048. Solar heating and cooling.

Perers, B. (1997). An improved dynamic solar collector test method for determination of non-linear optical and thermal characteristics with multiple regression. *Solar Energy*, *59*, 163 – 178. URL: http://www.sciencedirect.com/science/article/pii/S0038092X97001473. doi:https://doi.org/10.1016/S0038-092X(97)00147-3.

Quarteroni, A., Sacco, R., & Saleri, F. (2000). *Numerical Mathematics*. Springer.

Rodríguez-Muñoz, J. M., Monetta, A., Bove, I., & Alonso-Suárez, R. (2020). Ensayo cuasi-dinámico de colectores solares de placa plana en uruguay de acuerdo a la norma iso 9806:2017. *ENERLAC. Revista de energía de Latinoamérica y el Caribe*, *4*, 10–26. URL: http://enerlac.olade.org/index.php/ENERLAC/article/view/142.

Rojas, D., Beermann, J., Klein, S., & Reindl, D. (2008). Thermal performance testing of flat-plate collectors. *Solar Energy*, *82*, 746 – 757. URL: http://www.sciencedirect.com/science/article/pii/S0038092X08000352. doi:https://doi.org/10.1016/j.solener.2008.02.001.

Rönnelid, M., Perers, B., & Karlsson, B. (1997). On the factorisation of incidence angle modifiers for cpc collectors. *Solar Energy*, *59*, 281 – 286. URL: http://www.sciencedirect.com/science/article/pii/S0038092X97000169. doi:https://doi.org/10.1016/S0038-092X(97)00016-9. Selected Proceeding of ISES 1995: Solar World Congress. Part IV.

Souka, A., & Safwat, H. (1966). Determination of the optimum orientations for the double-exposure, flat-plate collector and its reflectors. *Solar Energy*, *10*, 170 – 174. URL: http://www.sciencedirect.com/science/article/pii/0038092X66900041. doi:https://doi.org/10.1016/0038-092X(66)90004-1.

Tesfamichael, T., & Wäckelgård, E. (2000). Angular solar absorptance and incident angle modifier of selective absorbers for solar thermal collectors. *Solar Energy*, *68*, 335 – 341. URL: http://www.sciencedirect.com/science/article/pii/S0038092X00000293. doi:https://doi.org/10.1016/S0038-092X(00)00029-3.

Zambolin, E., & Del Col, D. (2012). An improved procedure for the experimental characterization of optical efficiency in evacuated tube solar collectors. *Renewable Energy*, *43*, 37 – 46. URL: http://www.sciencedirect.com/science/article/pii/S0960148111006136. doi:https://doi.org/10.1016/j.renene.2011.11.011.